



OPEN Enhancing photothermal therapy effectiveness via tartrazine-induced optical clearing of biological tissues

Antonio Minopoli^{1,2}, Davide Evangelista^{1,2}, Matteo Marras^{1,2}, Giordano Perini^{1,2}, Alberto Augello^{2,3}, Valentina Palmieri³✉, Marco De Spirito^{1,2}✉ & Massimiliano Papi^{1,2}

Photothermal therapies offer a powerful strategy for noninvasive treatment of cancer and other pathological conditions by converting light energy into localized heat to ablate diseased tissues or induce local release of antigens. However, the efficacy and precision of these therapies are severely restricted by optical scattering in biological tissues, which limits light penetration and spatial accuracy *in vivo*. In this work, we leverage the food coloring dye tartrazine—a strongly absorbing molecule in UV-VIS range (~ 250 nm and ~ 430 nm) and with minimal absorption over 600 nm—to reduce tissue scattering and thereby enhance the delivery and efficacy of photothermal treatment. We demonstrate that when in aqueous environments, tartrazine induces local refractive index changes and minimizes the mismatch between water-based environments and lipid-rich tissue components, leading to a scattering reduction up to $\sim 65\%$ and enabling deeper light penetration and more homogeneous energy delivery. By incubating 3D samples with the dye, we achieved reversible optical clearing in *ex vivo* tissues, allowing near-complete light transmission through otherwise opaque sections. The enhanced optical accessibility directly improves the spatial resolution and energy deposition of photothermal therapies, potentially reducing off-target effects and tissue damage. Our results introduce a complementary perspective in photothermal therapy optimization, emphasizing that molecular absorption can play a central role beyond conventional thermal efficiency considerations. This refractive index-modulation opens the door to more targeted, efficient, and safe photothermal treatment protocols and offers a generalizable framework for light-based therapeutic applications in living organisms.

Thermal-based therapies exploit the biological response of tissues to elevated temperatures for therapeutic purposes^{1,2}. In particular, light-mediated hyperthermia offers a unique level of spatial and temporal control, enabling precise, minimally invasive interventions³. Among them, photothermal therapy (PTT) uses photo-absorbers capable of converting near-infrared (NIR) light into localized heat^{4–6}, inducing cell death through apoptosis, necrosis, or other regulated cell death pathways such as necroptosis^{7–10}. PTT can be distinguished into conventional high-temperature PTT—where temperatures exceed 50 °C—and mild photothermal therapy (MPTT), which operates below 45 °C and mitigate thermal damage to non-target tissues^{11,12}. PTT is effective in eradicating tumor masses; however, its clinical translation is hindered by relatively poor penetration depth due to the high scattering of biological tissues in the visible and NIR ranges, thermal diffusion to adjacent tissues, and the consequent heat shock response, which may strengthen tissue thermotolerance thereby reducing treatment efficacy¹³. In addition, the photo-absorbers commonly employed—such as gold nanostructures, graphene-based nanomaterials, or semiconducting polymers—exhibit suboptimal biocompatibility, limited biodegradability, and off-target accumulation *in vivo*^{14,15}.

To address these limitations, optical clearing techniques have been developed to reduce light scattering in biological tissues. These strategies typically rely on chemical agents that induce dehydration, lipid disruption, or refractive index matching between intra- and extracellular components, thereby enhancing optical transparency and improving the efficacy of light-based diagnostic and therapeutic techniques¹⁶. Nevertheless, many of the existing clearing agents (e.g., glycerol, DMSO, or hyperosmotic solutions) can compromise tissue integrity or induce cytotoxic effects, making them unsuitable for *in vivo* or translational applications¹⁶.

In this context, tartrazine (Tz)—a water-soluble azo dye widely used as a food additive—has recently attracted considerable attention for its unexpected ability to enhance tissue transparency. Tz is characterized by

¹Dipartimento di Neuroscienze, Università Cattolica del Sacro Cuore, Largo Francesco Vito 1, Rome 00168, Italy.

²Fondazione Policlinico Universitario A. Gemelli IRCSS, Rome 00168, Italy. ³Istituto dei Sistemi Complessi, CNR, Via dei Taurini 19, Rome 00185, Italy. ✉email: valentina.palmieri@cnr.it; marco.despirito@unicatt.it

strong absorption in the visible spectrum (400–500 nm), high solubility in aqueous environments, and a well-established safety profile, having long been approved for human consumption¹⁷. Following a groundbreaking study published by Ou et al. 2024, where Tz was identified as a key molecule in inducing rapid, reversible and non-destructive optical clearing, its application in biomedical optics has become an emerging field of research^{18–20}. Briefly, Ou et al. 2024 demonstrated that Tz dissolved in water induces a significant increase in the real part (n') of the refractive index (RI) of the aqueous medium at wavelengths longer than 600 nm. From a physical point of view, scattering in tissue arises from local RI mismatches between aqueous phases ($n' \approx 1.33$) and high-index structures such as lipids and proteins ($n' \approx 1.43$ – 1.53). Traditional approaches to enhance light penetration rely either on using longer wavelengths—where Rayleigh scattering decreases with λ^{-4} —or on chemical clearing agents that remove/replace tissue components. In contrast, Tz represents a fundamentally different strategy, grounded in the theoretical physics of light–matter interactions²¹. According to the Lorentzian oscillator model and the Kramers–Kronig relations, molecules with strong absorption in the near-UV (300–400 nm) or violet/blue range (400–470 nm) can induce an elevation of the RI at longer, red-shifted wavelengths where tissues are relatively transparent. Tz, with its intense absorption in the 400–500 nm range, functions as a near-resonance Lorentzian oscillator: it increases the RI of the aqueous phase at $\lambda > 600$ nm, thereby reducing RI contrast with lipids and proteins. This index matching suppresses Mie scattering from subcellular structures, allowing photons to propagate more deeply and homogeneously without chemically altering or damaging native biomolecules. Nevertheless, while its clearing effects have been demonstrated in imaging applications, its potential to overcome one of the main barriers limiting PTT—poor light penetration in tissue—remains largely unexplored. This is the first study to directly investigate whether Tz-mediated optical clearing can improve the therapeutic efficacy of PTT.

In this study, we explore the optical clearing properties of Tz and its ability to reduce light scattering in biological tissues. We hypothesize that Tz can enhance tissue transparency by interacting with structural components of the extracellular matrix (ECM), thereby facilitating improved light delivery for PTT. We assess tissue optical properties following Tz treatment using spectrophotometric and imaging-based approaches and examine whether Tz pre-treatment enhances the efficacy of photothermal heating. Unlike conventional clearing agents, which compromise tissue integrity, Tz combines effective clearing with a proven safety profile, making it uniquely suitable for translation to in vivo applications, particularly in scenarios requiring deeper or more uniform light penetration.

Materials and methods

Chemicals and materials

Tartrazine (IUPAC trisodium 1-(4-sulfonatophenyl)-4-(4-sulfonatophenylazo)-5-pyrazolone-3-carboxylate) (> 99%, Sigma-Aldrich T0388, St. Louis, MO, USA) was used as dye molecule in this study. Scattering agents were 1- μ m diameter polystyrene beads (72938, Sigma-Aldrich, St. Louis, MO, USA) at 2% solid (20 mg/ mL), 20-nm diameter polystyrene beads (NIST standard 3020 A, Duke Scientific Corporation, Whaltam, MA, USA) at 1% (10 mg/ mL) and turbidity 4000 NTU calibration standard-formazin (TURB4000, Sigma-Aldrich, St. Louis, MO, USA). Agar (A5054, Sigma-Aldrich, St. Louis, MO, USA) was used to prepare tissue mimicking phantoms. Sodium alginate (W201502) and alginate lyase (A1603, ≥ 10000 U/g) were purchased from Sigma-Aldrich (St. Louis, MO, USA). U87 human glioblastoma multiforme (GBM) cells were purchased from the American Type Culture Collection, (ATTC, Manassas, VA, USA). Cells were maintained in Dulbecco's modified Eagle's medium (DMEM) without phenol red (Sigma-Aldrich, St. Louis, MO, USA), supplemented with 10% fetal bovine serum (FBS, EuroClone, Milan, Italy), 2% penicillin-streptomycin (Sigma-Aldrich, St. Louis, USA). Photo-absorber scaffolds used in photothermal experiments were 3D printed using a polylactic acid (PLA) filament with 5% graphene (PLA/G). This filament has demonstrated extremely low cytotoxicity in a previous work²². Calcein-AM (Invitrogen, MA, USA) and propidium iodide (Sigma-Aldrich, MO, USA) were used to stain living and dead cells respectively. ROS-ID Total ROS/Superoxide Detection KIT (Enzo Life Sciences, NY, USA) was used to assess ROS production. Vybrant Apoptosis Assay Kit (Invitrogen, MA, USA) was used to observe apoptotic cells.

Optical response of scattering phantoms (finite-difference time-domain method)

The optical response of the scattering phantoms was simulated by using the finite-difference time-domain (FDTD) method implemented in “FDTD solutions” tool of Lumerical-Ansys software. The Maxwell's equations are numerically solved in the time domain within a Mie problem-like framework by discretizing the space over a mesh evaluating the evolution of the electromagnetic field in each cell. An illustration of the simulation workspace is shown in Fig. 1a. The source consisted of x -polarized wave of wavelength 808 nm propagating along z direction. A photodetector of size $1 \times 1 \mu\text{m}^2$ placed in the yz plane was dedicated to measure the electric field over time, whereas a second photodetector positioned on the opposite side of the workspace was set to collect the transmitted photons to work out the output power. The scattering phantoms were realized by randomly positioning homogeneous polystyrene (PS) spheres of diameter 1 μ m and 20 nm, and RI 1.578 into an agarose volume of size 10 μ m and RI 1.336. Perfectly matched layer boundary conditions (steep angle profile, 12 layers) warranted the complete absorption of the wave backscattered through the light source and that traveling beyond the photodetector. The spatial resolution of the mesh was set equal to 10 nm to warrant high accuracy of the results while holding the simulation time within few hours.

Water-based scattering solutions

To prepare water-based scattering solutions, 10 mL of distilled water (dH_2O) was preheated at 40 °C under vigorous stirring to allow Tz to dissolve more easily. A stock solution of Tz at 0.9 M was prepared dissolving 4.8 g of Tz in 10 mL of dH_2O . Lower Tz concentrations down to 0.001 M were obtained through serial dilutions. After Tz dissolution, solutions were cooled at room temperature and scattering agents at different concentrations were

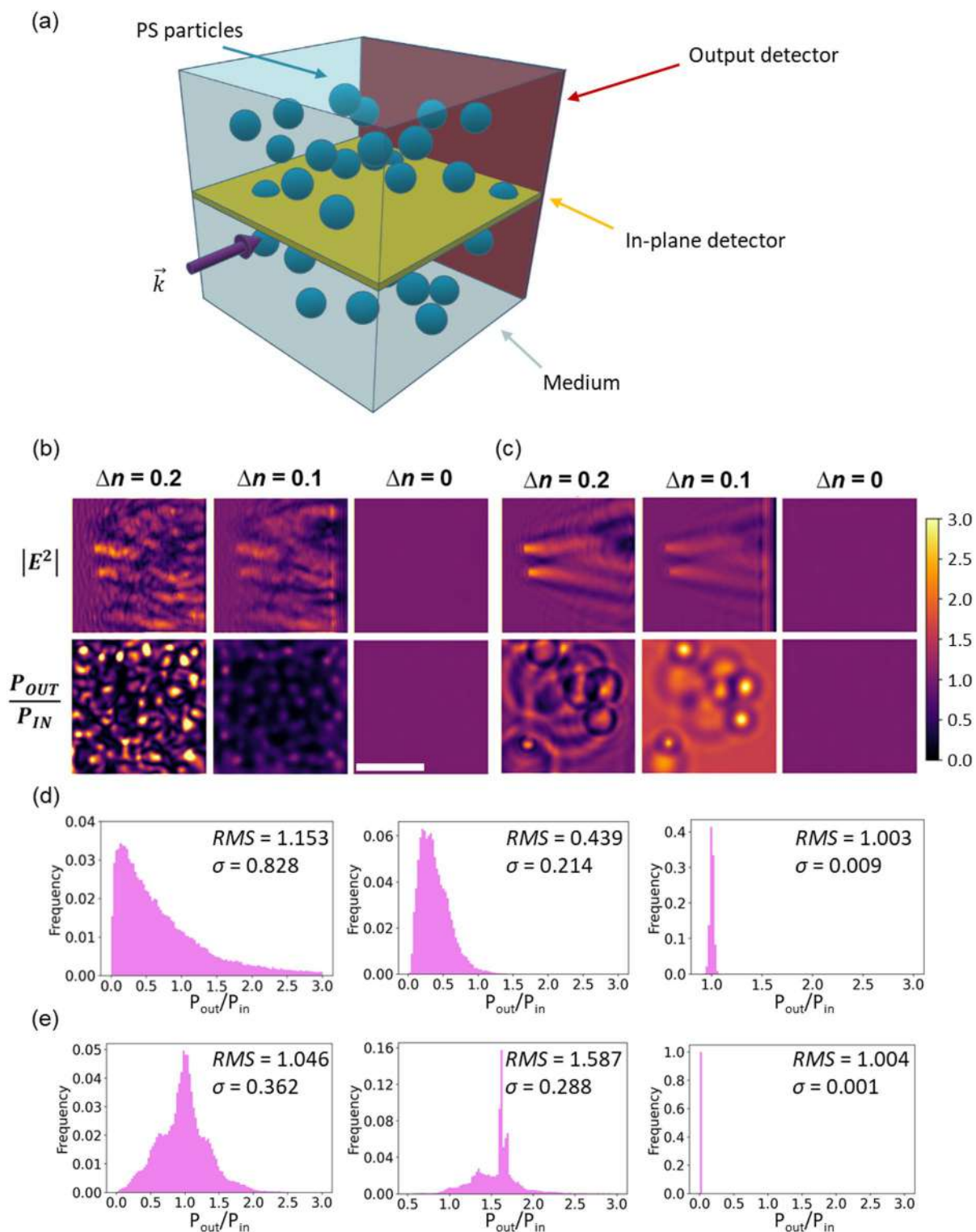


Fig. 1. (a) Sketch of the simulation workspace consisting of linearly polarized electromagnetic wave, in-plane and output detectors, PS particles and embedding medium. (b, c) In plane E-field intensity distributions (top panels) and normalized output power distributions (bottom panels) in the case of 1- μm PS particles at concentrations of $3 \cdot 10^8$ and $3 \cdot 10^7$ particles/ mm^3 , respectively. Scale bar = 5 μm . (d, e) Corresponding histograms of the normalized output powers in the case of 1- μm PS particles at concentrations of $3 \cdot 10^8$ and $3 \cdot 10^7$ particles/ mm^3 , respectively.

added under vigorous stirring. The scattering agents included: 1- μm diameter PS beads (investigated range 0.02–4 mg/mL), 20-nm diameter PS beads (0.01–2 mg/mL), 4000 NTU turbid solution (from 1:1000 to 1:5 ratio of the stock solution). Scattering solutions were then transferred into a 96-well plate for optical analysis. Measurements were carried out using Cytation3 Cell Imaging Multi-Mode Reader (BioTek). Optical density (OD) was measured as an indicator of the light absorbance. Results were compared with the corresponding scattering solutions without Tz molecules. To quantify the impact of Tz on the optical properties of the solutions under NIR laser exposure, the ratio of OD at 808 nm between dye-free and dye-containing samples was calculated.

Scattering phantoms Preparation

To replicate the optical properties of biological tissues, agarose hydrogels (6 mg/mL) embedding scattering particles were employed. Agarose was selected because it forms a stable, optically homogeneous gel widely used to mimic the mechanical and optical properties of soft tissues, and the 6 mg/mL concentration provides a solid and stable matrix while minimally affecting the RI, keeping it close to that of water²³. Optimal concentrations for both Tz and scattering agents were selected from optical results on water-based scattering solutions. Agarose phantoms were prepared preheating 10 mL of dH_2O at 85 °C and adding 66 mg of agarose under vigorous stirring. Keeping the temperature and stirring constant, Tz and scattering agents were sequentially added to the desired concentration until complete dissolution and dispersion, respectively. A volume of 100 μL of solution was then poured into a 96-well plate and cooled at room temperature allowing the agarose to crosslinking. A volume of 100 μL of cell culture medium DMEM without phenol red was added into each well prior to the optical measurement.

To evaluate the improvement of images acquired through Tz-treated phantoms in terms of contrast-to-noise ratio (CNR) and signal-to-noise ratio (SNR), 1.85 mL of solutions at agarose concentration of 6 mg/mL and embedding 1- μm PS beads at 0.2 mg/mL, 20-nm PS beads at 1 mg/mL, and NTU at 1:1000 dilution ratio were molded in glass Petri dishes of diameter 28 mm. The thickness of the resulting phantoms was 3 mm. Tz concentrations for treated phantoms were 0.3 M and 0.5 M.

To evaluate heat transmission through scattering phantoms, agarose disks of thickness 4 mm and 6 mm were molded into a 6-well plate pouring 5 mL and 7.5 mL, respectively, of agarose solutions (Tz concentrations 0.3 M and 0.5 M, 1- μm PS beads 0.2 mg/mL). PLA/G disks were placed on the bottom of the well prior to pour agarose solutions. Tz-untreated phantoms were used as control. The phantoms were irradiated using an 808 nm diode laser (Civil Laser Manufacturer) at power densities of 0.37 W/cm², 0.49 W/cm², 0.62 W/cm², 0.75 W/cm², and 1.06 W/cm². Thermal images were captured with an NIR camera (Optris). Temperature-time curves were measured from the irradiated spot.

Treatment of ex vivo tissue

The impact of Tz dye on optical transparency was further assessed ex vivo using fresh chicken muscle tissues of average thickness 3 mm purchased from a local butcher. Chicken samples were soaked in Tz solutions at two different concentrations (0.3 M and 0.5 M). OD distributions of the samples at wavelengths 560 nm, 615 nm, and 808 nm were collected over a 25 \times 25 matrix after 2 h, 8 h and 24 h of soaking in Tz. Samples were kept at room temperature for the whole measurement process. Untreated chicken samples were soaked in dH_2O as control.

To evaluate heat transmission through ex vivo tissues, chicken samples were soaked in Tz solutions at concentrations 0.3 M and 0.5 M for 2 h, whereas untreated samples were soaked in dH_2O . Untreated and Tz-treated chicken samples were then transferred into a 6-well and placed onto a PLA/G disk. Silicon o-rings of diameter 35 mm were used to keep the chicken samples at the bottom of each well. Laser spot was pointed at PLA/G disks for 180 s at different laser power densities (0.37 W/cm², 0.49 W/cm², 0.62 W/cm², 0.75 W/cm², 1.06 W/cm²). Temperature-time curves were measured from the irradiated spot.

Image analysis

To evaluate image quality, resolution patterns of thickness 3.0 mm, 2.5 mm, 2.0 mm, 1.5 mm, 1.0 mm, 0.5 mm were acquired through 3-mm thick agarose phantoms and 3-mm thick ex vivo chicken tissue. Images were acquired under a controlled lighting environment to ensure uniform illumination and minimize external interference. Image analysis was performed using ImageJ. CNR and SNR were defined as²⁴:

$$CNR = \frac{|I_{\text{white}} - I_{\text{black}}|}{\sigma_0} \quad (1)$$

$$SNR = \frac{I_{\text{black}}}{\sigma_{\text{black}}} \quad (2)$$

where I_{white} and I_{black} are the average pixel values of white and black bands, respectively, σ_0 is the standard deviation of the blank image noise, and σ_{black} is the standard deviation of the black band. We limited the image analysis to a central region of interest of size 20 \times 20 mm² to exclude image distortions.

Heat transfer in porous media (finite element method)

To infer the heat distribution within the agarose phantoms achieved at different laser power, we numerically solved the heat-conduction Fick's equation in COMSOL Multiphysics. Figure 5e shows a scheme of the simulation workspace consisting of an agarose cylinder (height 4 mm, radius 10 mm) lying on a PLA/G disk (radius 2 mm, thickness 0.5 mm, density 1.3 g/cm³, thermal conductivity 1 W·m⁻¹·K⁻¹), on which the laser power is deposited, and surrounded by a water layer of thickness 4 mm. Agarose disk was modeled as a porous medium with porosity 70%^{25,26}, thermal conductivity of 0.57 W/(m·K)²⁷, density 1.1 g/cm³²⁷, and viscosity 1

kPa²⁸. The deposited beam power on the PLA/G disk was set at 0.7 W/cm² with a Gaussian beam profile ($\sigma = 4$ mm), according to the experimental conditions. The initial temperature of the system was set at 20 °C, whereas the remaining domains/interfaces could freely transfer the heat. The meshing was adaptive and chosen to be finer close to the phantom/disk interface. Temperature distributions were evaluated in the *xz* plane after 180 s of irradiation with laser powers of 0.37 W/cm², 0.49 W/cm², 0.62 W/cm², and 0.75 W/cm², 1.06 W/cm².

3D Bioprinting of GBM tumoroids

GBM tumoroids were fabricated via extrusion-based bioprinting (Bio X, CELLINK) and chemical crosslinking. Specifically, the bioink was prepared by mixing U87 cells with alginate (2% w/v) in ratio 1:2 to obtain a final cell concentration of 10⁶ cells/mL. Alginate was selected because it closely mimics the mechanical and optical properties of brain tissue²⁹ and is widely employed in *in vitro* neuro-oncology models, thus providing a relevant substrate for the optical assessments performed in this study^{30,31}. A volume of 50 μ L was extruded into 3D printed holders of PLA/G and crosslinked with 3% calcium chloride for 2 min. GBM tumoroids were kept in cell culture medium at 37 °C for 24 h prior to NIR irradiation.

Irradiation of GBM model

GBM tumoroids were irradiated with 808-nm NIR laser at power densities of 0.37 W/cm², 0.62 W/cm², and 1.06 W/cm² for 180 min placing a glass Petri dish containing untreated and Tz-treated agarose phantoms between the laser source and the GBM model. Non-irradiated GBM models were used as control group. GBM models were stained with live/dead assay 2 hours after NIR irradiation. In detail, calcein-AM, capable of staining live cells, and propidium iodide (PI), capable of staining dead cells, were added to the culture medium at a final concentration of 5 μ M. After 20 min of incubation at 37 °C, fluorescence at excitation/emission wavelengths of 495/515 nm (calcein-AM) and 535/617 nm (PI) was acquired using Cytation 3 Cell Imaging Multi-Mode Reader (BioTek).

Oxidative stress following NIR irradiation was assessed using a ROS-ID[®] detection kit. Immediately after laser exposure, 100 μ L of GBM tumoroid supernatant was collected. Oxidative stress detection reagent was added at a 1:2500 dilution and incubated for 60 min at 37 °C in dark conditions. Fluorescence was then measured using Cytation 3 Multi-Mode Reader at excitation/emission wavelengths of 488/520 nm.

Apoptosis was quantified using the Vybrant[®] Apoptosis Assay Kit. Prior to staining, GBM cells were recovered from the alginate matrix using enzymatic digestion. Briefly, tumoroids were rinsed with PBS, and alginate lyase (0.1 mg/mL) was added at a volume 10 times the sample size, followed by incubation at 37 °C for 60 min. The resulting suspension was passed through a 70 μ m nylon cell strainer, centrifuged, and the cell pellet was resuspended in 100 μ L of 1X annexin-binding buffer. Next, 5 μ L of biotin-X annexin V was added and incubated for 15 min at room temperature. Samples were then centrifuged, washed, and stained with 1 μ L of 1 mg/mL Alexa Fluor 350 streptavidin solution, followed by a 30-minute incubation. After rinsing, 1 μ L of 1 mg/mL PI was added and incubated for 6 min at room temperature. Fluorescence intensity was recorded at excitation/emission wavelengths of 365/440 nm (Alexa Fluor 350) and 535/617 nm (PI), using Cytation 3 Multi-Mode Reader.

Results and discussion

In Silico investigation of optical properties of scattering phantoms

To understand how the RI mismatch between scatters and surrounding medium affect the solution transparency, we performed computational simulations based on finite-difference time-domain (FDTD) method. To this aim, we built a three-dimensional in-silico workspace consisting of PS beads of RI 1.578 embedded in aqueous solution whose RI was systematically varied to simulate different Tz concentrations. The RI values were selected to match experimentally measured changes at specific Tz concentrations, which exhibits a linear dependence of + 0.125 RI units per molar at 800 nm wavelength^{21,23}, allowing the simulations to accurately represent the optical conditions induced by varying Tz levels. In addition, we varied beads size (20 nm and 1 μ m) and beads density (3·10⁸ beads/mm³ and 3·10⁷ beads/mm³) to have a comprehensive overview. Figure 1a shows the simulation workspace consisting of a scattering phantom, a linearly polarized electromagnetic source and two detectors dedicated to evaluating the in-plane electric field intensity and the transmitted power. As expected, a reduction in the RI mismatch between scatters and surrounding medium resulted in a more homogeneous E-field intensity and transmitted power distributions for 1 μ m PS beads (Fig. 1b and d). Interestingly, such an effect is much less pronounced when 1 μ m PS beads were replaced with 20 nm PS beads because of their lower scattering cross section and smaller impact on the effective phantom RI (Fig. S1)^{32,33}. Lastly, Fig. 1c and e shows that Tz treatment impacts much more on densely packed scattering phantoms compared to plainer phantoms opening captivating opportunities in optically clearing biological tissues to enhance light penetration for both diagnostic and therapeutic purposes.

Tz-induced enhancement of optical transparency

To assess the effectiveness of Tz in enhancing optical clarity of biological tissues, we firstly selected water-based samples with different scattering agents: (i) PS microbeads of diameter 1 μ m, (ii) PS nanobeads of diameter 20 nm, and (iii) 4000 NTU standard turbid solution. Figure 2a shows the absorption spectra of Tz-treated scattering samples at Tz concentrations of 0 M (control), 0.05 M, 0.3 M and 0.9 M (absorption spectra at all Tz concentrations are shown in Fig. S2).

The investigated samples show similar trends with increasing transmittance in the range 600–900 nm as the Tz concentration increases with a pronounced hook effect at Tz concentrations larger than 0.9 M due to the excessive solution opacity. Considering the potential interest in using Tz for enhancing PTT effectiveness, we evaluated the enhancement factor (EF) of optical transmittance achieved in Tz-treated samples at 808 nm, a wavelength typically used in PTT treatments:

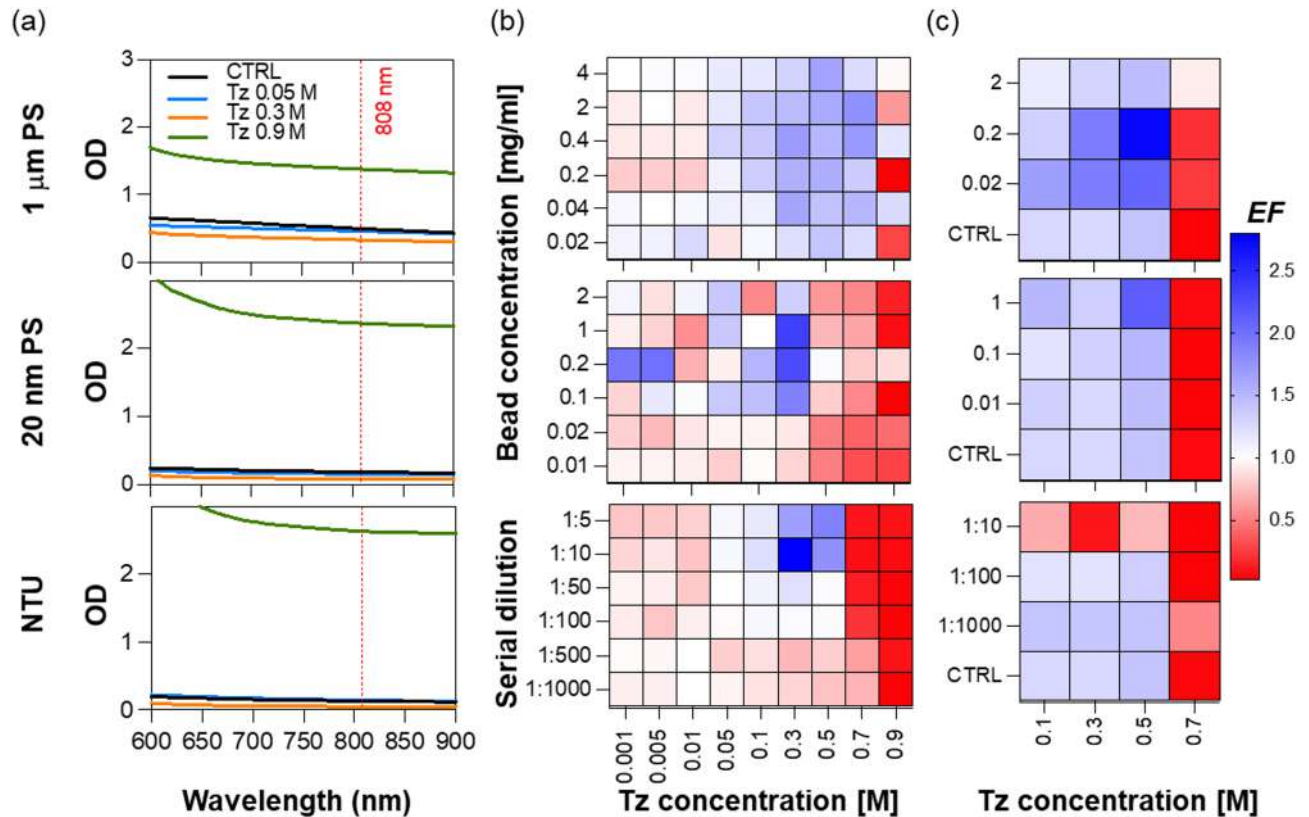


Fig. 2. (a) Absorption spectra of Tz-treated and untreated scattering samples containing 1- μ m PS beads (top panel), 20-nm PS beads (middle panel), 4000 NTU standard turbid solution (bottom panel). (b, c) EF values measured as the ratio of optical densities at 808 nm between untreated and Tz-treated water-based scattering samples and agarose scattering phantoms. Data are reported as mean value on three independent measurements.

$$EF = \frac{OD_{808}^{CTRL}}{OD_{808}^{Tz}} \quad (3)$$

where OD_{808}^{Tz} and OD_{808}^{CTRL} are the optical densities (OD) measured at 808 nm in the case of Tz-treated and control samples respectively. Figure 2b shows the EF values yielded for different conditions of scattering agents dispersed in water as a function of Tz concentration. The EF values exhibit a pronounced increase at Tz concentrations higher than 0.05 M with a marked effect in the range 0.3–0.5 M. Higher Tz concentrations caused the clotting of the solution and excessive opacity thus resulting detrimental for enhancing its optical transparency.

Cross-referencing the data for each scattering condition, we can identify convenient regions to focus on for following studies. Specifically, solutions containing PS beads of 1- μ m diameter exhibit an extended region with EF values larger than 1, spanning over Tz concentrations in the range 0.05–0.7 M and beads concentrations in the range 0.02–4 mg/mL. In contrast, solutions containing PS beads of 20-nm diameter exhibit a narrower region (Tz concentrations 0.05–0.3 M, beads concentrations 0.01–2 mg/mL) due to the larger mismatch between the RI of Tz dyes and 20-nm PS beads. Lastly, turbid solutions exhibit an EF distribution with higher degree of randomness due to its inherent dust composition, with a convenient region ($EF > 1$) in Tz concentration range of 0.05–0.5 M.

Aiming to mimic the in vivo conditions closer and to replicate light scattering in human tissues, we moved to agarose phantoms in which the scattering agents were homogeneously dispersed^{32,34}. Figure 2c shows the EF distributions of Tz-treated agarose phantoms at different Tz and scattering concentrations. Again, we can outline regions with EF values larger than 1. While the optical transparency of agar phantoms with PS beads (both 20-nm and 1- μ m diameter) enhances when treated with 0.1–0.5 M of Tz regardless of bead concentrations, agarose phantoms with 4000 NTU standard turbid solution required at least 1:100 dilution from the stock turbid solution to appreciate an improvement in the EF values.

The EF distributions in both water-based samples and agarose phantoms confirm that the Tz treatment leads to a competitive effect: on the one hand reduction of the RI mismatch and, hence, of the scattering cross section up to $\sim 65\%$, on the other hand increase of Tz dye absorption itself. Therefore, at high concentrations of Tz (consistently larger than 0.7 M) the Tz absorption dominates over the reduction of the scattering cross section, thereby resulting in a competitive hook effect. Data suggest that concentrations of 0.2 mg/mL for 1- μ m PS

beads, 1 mg/mL for 20-nm PS beads and 1:1000 for turbid solution are ideal to study clearing efficacy at a Tz concentration of 0.5 M, which consistently enhanced the optical transparency of the samples.

Lastly, we explored the optical properties of Tz-treated chicken tissues of thickness 3 mm. Figure 3a and b shows the two-dimensional distributions of optical absorption at different wavelengths in the visible and NIR range through chicken tissues treated with Tz at concentrations of 0.3 M and 0.5 M. Tz-treated chicken tissues exhibit higher optical transparency compared to untreated samples with 1.7-fold, 1.4-fold, and 1.4-fold enhancement at 560 nm, 615 nm, and 808 nm, respectively (Fig. 3c). We monitored the optical absorption of these samples over time confirming the biochemical stability of Tz in ex vivo tissue (Figs. 3d and S3).

To assess the reversibility of the Tz treatment in ex vivo tissue, we transferred 0.5 M Tz-treated chicken sample into dH₂O overnight and measured OD at 560 nm, 615 nm, and 808 nm. Results showed an increase of OD to values comparable to those measured in control group in Fig. 3c due to the release of Tz molecules from the samples (Fig. S4).

Tissue optical quality after Tz clarification

We evaluated optical quality of images acquired through 3-mm thick agarose phantoms embedding the different scatters at concentrations 0.2 mg/mL (1- μ m PS beads), 1 mg/mL (20-nm PS beads), and 1:1000 diluted turbid solution. Figure 4a shows representative pictures of the 1-mm resolution pattern pictured through the 1- μ m PS agarose phantoms, in which the improved image sharpness through the Tz-treated phantoms is strikingly evaluable even by naked eye. The intensity profiles measured across the pattern lines reveal a significant signal smoothing—i.e., improved image denoising—in the case of Tz-treated phantoms (Fig. 4b).

To assess the actual improvement of the image quality, we evaluated the SNR and the CNR of patterns of gradually reduced size acquired through 3 mm-thick Tz-treated and untreated phantoms embedding the different scatters. We defined the gains Y for SNR and CNR as the ratio between the quality descriptors in Tz-treated phantom and untreated phantom:

$$Y_{\text{SNR}} = \frac{\text{SNR}_{\text{Tz}}}{\text{SNR}_{\text{CTRL}}} \quad (4)$$

$$Y_{\text{CNR}} = \frac{\text{CNR}_{\text{Tz}}}{\text{CNR}_{\text{CTRL}}} \quad (5)$$

The gain distributions in Fig. 4f show a consistent improvement of the image contrast (CNR) regardless of the scatter type, whereas a pronounced improvement of the image resolution (SNR) only using 1- μ m PS phantoms. Indeed, SNR and CNR histograms measured with 1 μ m PS phantoms show a consistent enhancement of both image sharpness and contrast down to 0.4 mm pattern resolution (Fig. 4g). This corroborates the previous results in which we observed a more pronounced effect in tissue clarification when larger scatters are embedded.

We further extended our evaluation to ex-vivo chicken samples to assess whether the clearing effect of Tz translates into more realistic biological samples. As shown in Fig. 4c, the visibility of the resolution pattern progressively improved as the Tz concentration increased. This enhancement is quantitatively supported by the intensity profiles in Fig. 4d, which reveal sharper signal transitions and reduced background noise after Tz treatment at 0.5 M. Correspondingly, the CNR values increased with rising Tz concentration (Fig. 4e), confirming a consistent improvement in image contrast. These results suggest that Tz-mediated RI matching can significantly reduce scattering in complex, heterogeneous tissues, enabling deeper and clearer optical visualization.

Heat diffusion through tissue-mimicking phantoms and ex vivo models

For the following studies focused on evaluating the heat diffusion in tissue-mimicking phantoms, we selected agarose phantoms embedding 1 μ m PS beads and treated with Tz concentrations of 0.3 M and 0.5 M. The setup adopted throughout this section consists of an 808-nm NIR laser pointing the sample lying on a PLA/G disk as photo-absorber while images were acquired with a thermal camera. Temperature changes in 4-mm and 6-mm phantoms were recorded over 180 s of NIR exposure at a laser power of 0.37 W/cm², 0.49 W/cm², 0.62 W/cm², and 0.75 W/cm², 1.06 W/cm². Such laser powers were empirically selected to approach temperatures that allowed us to explore three different regimes: (i) control, (ii) MPTT, (iii) PTT. Specifically, untreated phantoms of thickness 4 mm approached a maximum temperature of 45.4 °C after 180 s of irradiation at 1.06 W/cm², whereas 0.3 M and 0.5 M Tz-treated phantoms reached 51.6 °C and 55.0 °C, respectively (Fig. 5a). These temperature raises would correspond to a gain in photothermal effectiveness of approximately 14% and 21%, respectively.

A less pronounced thermal gain was observed for thicker phantoms of 6 mm (Fig. 5b). Specifically, temperatures approached after 180 s of NIR irradiation at 1.06 W/cm² were 34.2 °C in untreated phantoms, while 35.9 °C and 38.3 °C in 0.3 M and 0.5 M Tz-treated phantoms, respectively, corresponding to a gain of \approx 5%, and 12%, respectively. This reduced effect at higher thickness is likely due to stronger optical attenuation and thermal dissipation in larger phantom volumes: as thickness increases, light penetration is progressively limited by scattering, lowering the local fluence delivered to deeper regions. In addition, the greater thermal mass of thicker phantoms promotes heat diffusion away from the irradiated area, thereby reducing the net temperature rise even in the presence of Tz.

Both in PTT and MPTT regimes, NIR irradiation gave rise to a relatively smooth temperature gradient over the agarose disk. For example, at a power density of 0.62 W/cm² the temperature moved from 37 °C in close contact with the photothermal emitter to 27 °C in the apical region, ca. 2 °C/mm, whereas from 47 °C to 27 °C (ca. 2.8 °C/mm) with a laser power of 0.75 W/cm², being a crucial aspect to equalize and maximize the biological effectiveness over the region during the NIR laser treatment. Figure 5c shows two representative thermal images of agarose phantoms undergone 180-s photothermal irradiation at 0.75 W/cm².

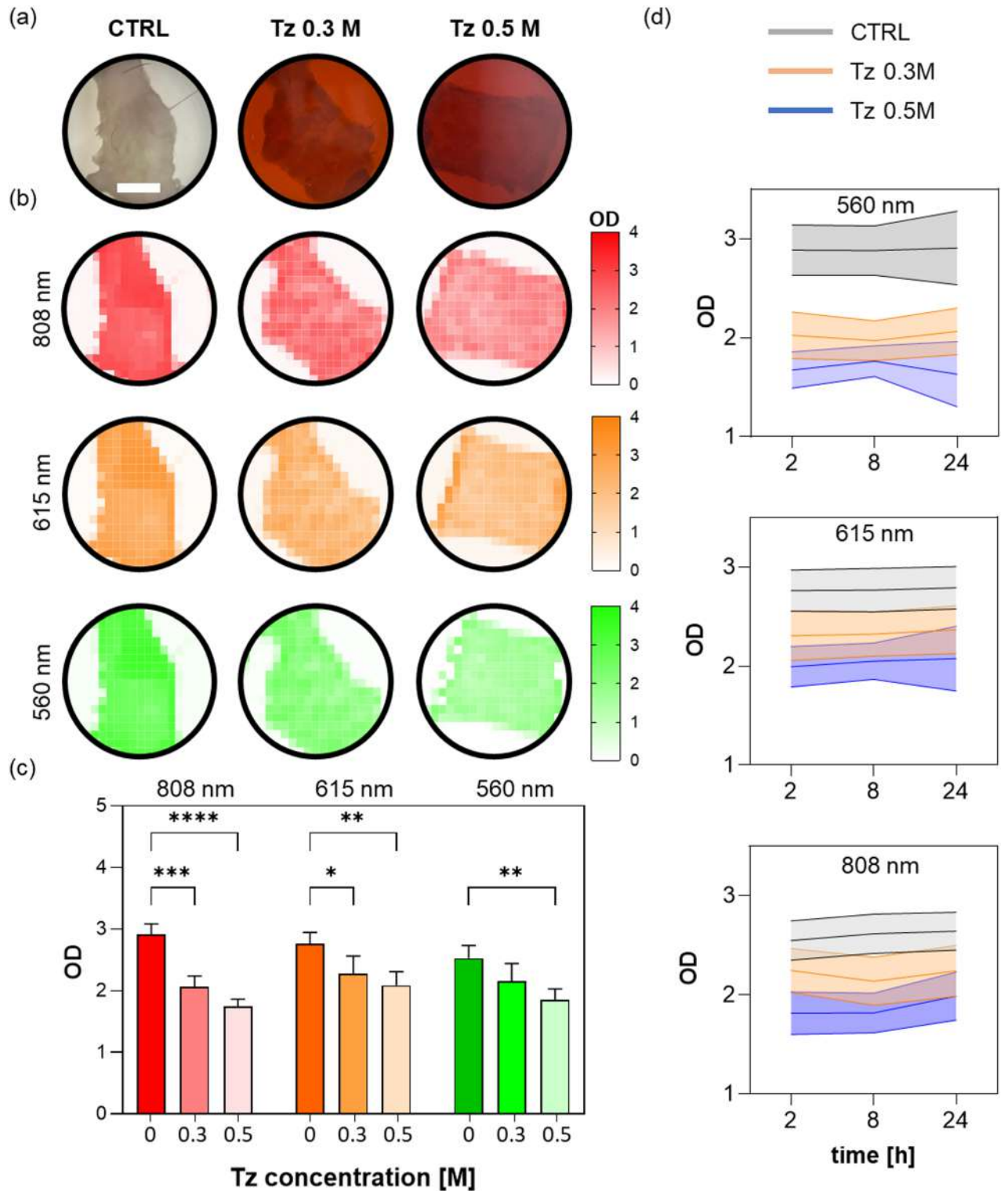


Fig. 3. (a) Optical images and (b) OD distributions at wavelengths 560 nm, 615 nm, and 808 nm of untreated and Tz-treated chicken samples after 2 h of soaking in Tz solution. Scale bar = 10 mm. (c) Histograms of the mean OD values measured through chicken samples after 2 h of soaking in Tz solution. Data are reported as mean value \pm standard deviation on three independent measurements. Statistical significance was evaluated using two-way ANOVA test ($p > 0.05$; * $p < 0.05$; ** $p < 0.01$; *** $p < 0.001$; **** $p < 0.0001$). (d) Mean OD values monitored over 24 h. Data are reported as mean value \pm standard deviation on three independent measurements.

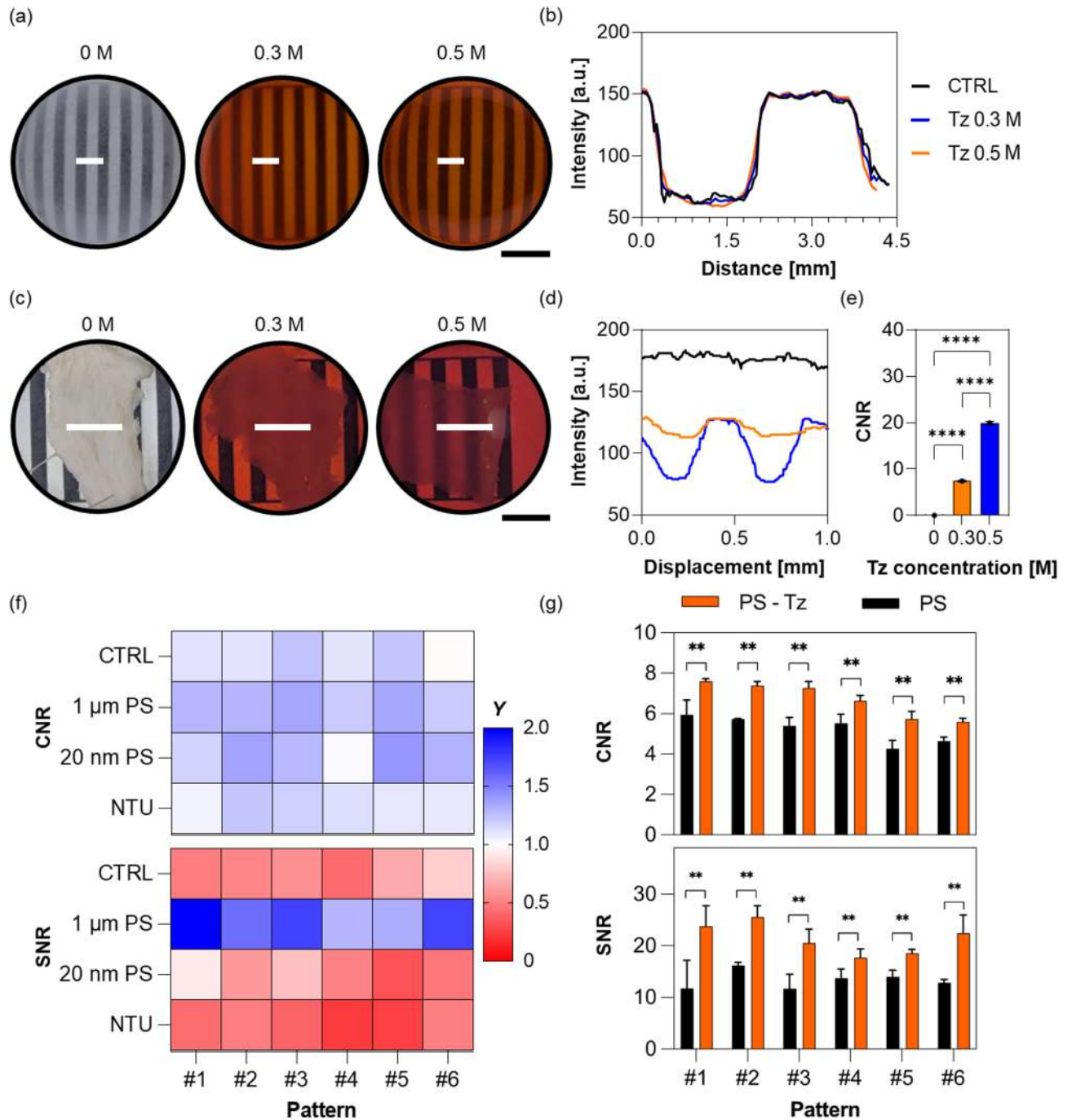


Fig. 4. (a) Representative pictures of the 1-mm resolution pattern acquired through 3-mm thick agarose phantoms embedding 1- μ m PS beads at a concentration of 0.2 mg/mL. Scale bar = 10 mm. (b) Intensity profiles evaluated across the horizontal white lines highlighted in panel (a). (c) Representative pictures of untreated and Tz-treated chicken samples after 2 h of soaking in Tz solution. Scale bar = 10 mm. (d) Intensity profiles evaluated across the horizontal white lines highlighted in panel (c). (e) CNR values evaluated on the resolution pattern of thickness 3.0 mm. Data are reported as mean value \pm standard deviation on three independent measurements. Statistical significance was evaluated using one-way ANOVA test (**** $p < 0.0001$). (f) CNR and SNR values evaluated on resolution patterns of decreasing thickness (from pattern #1 to pattern #6: 3.0 mm, 2.5 mm, 2.0 mm, 1.5 mm, 1.0 mm, 0.5 mm) through agarose phantom embedding 1- μ m PS beads (0.2 mg/mL), 20- μ m PS beads (1 mg/mL), and NTU (1:1000 diluted). Data are reported as mean value \pm standard deviation on three independent measurements. (g) CNR and SNR values of the resolution patterns acquired through agarose phantom embedding 1- μ m PS beads at a concentration of 0.2 mg/mL. Data are reported as mean value \pm standard deviation on three independent measurements. Statistical significance was evaluated using paired t -test with 95% confidence interval (** $p < 0.01$).

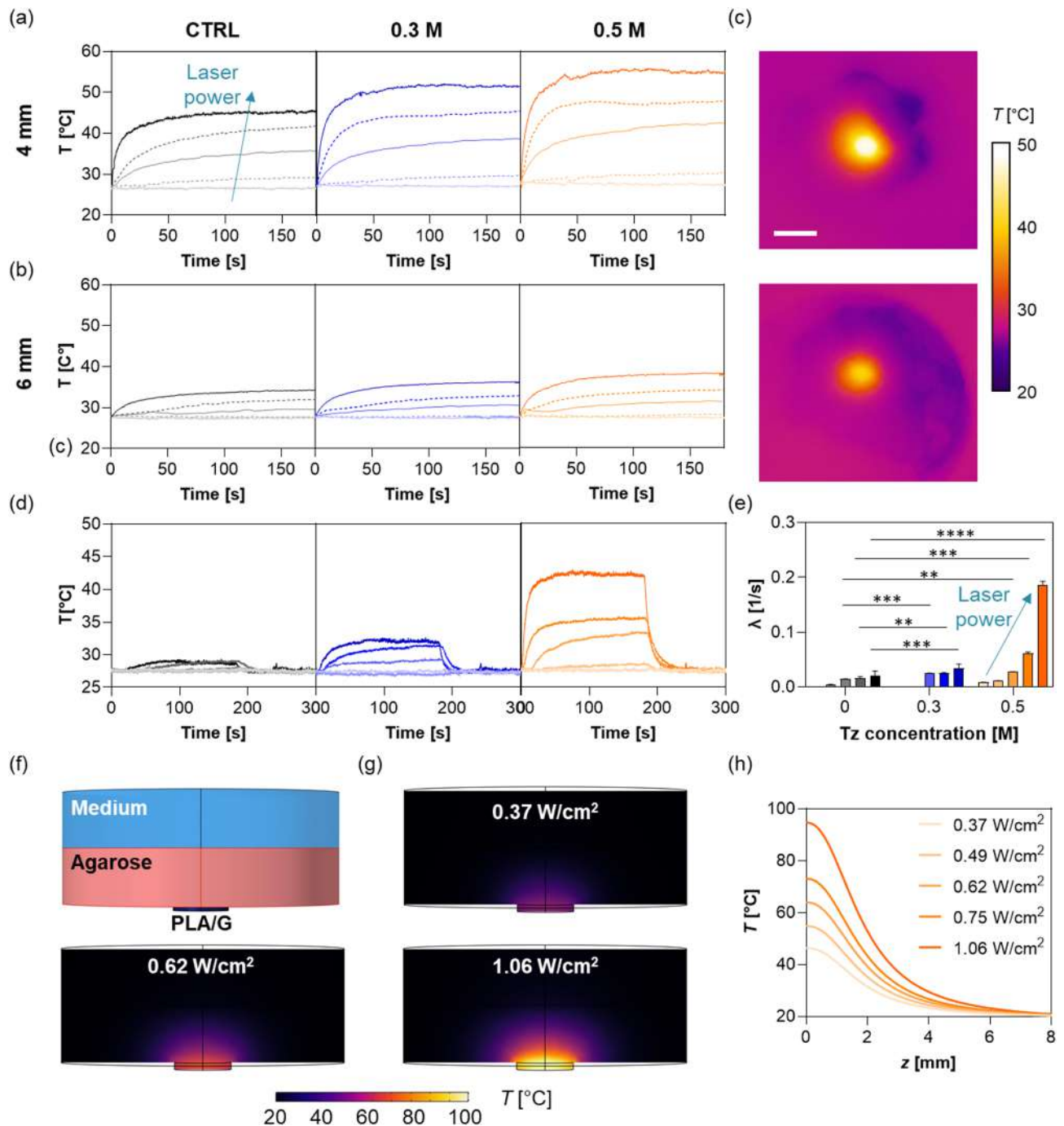


Fig. 5. Peak temperature over time measured on agarose phantom of thickness (a) 4 mm and (b) 6 mm at different laser power densities (according to the arrow direction: 0.37 W/cm², 0.49 W/cm², 0.62 W/cm², 0.75 W/cm², 1.06 W/cm²). (c) Representative thermal images of agarose 4-mm (top panel) and 6-mm thick (bottom panel) agarose phantoms after 180 s of laser irradiation at 0.75 W/cm². Scale bar = 2 mm. (d) Peak temperature over time measured on ex vivo chicken muscle tissues of average thickness 3 mm at different laser power densities (0.37 W/cm², 0.49 W/cm², 0.62 W/cm², 0.75 W/cm², 1.06 W/cm²). (e) Corresponding λ values obtained by fitting with Eq. (6) the thermal responses recorded in panel (d). Data are reported as mean value \pm standard deviation on three independent measurements. Statistical significance was evaluated using two-way ANOVA test (** $p < 0.01$; *** $p < 0.001$; **** $p < 0.0001$). (f) Sketch of the simulation workspace consisting of PLA/G disk as thermal photoemitter, agarose disk and cell culture medium. (g) Temperature distributions in the xz plane at laser power densities of 0.37 W/cm², 0.62 W/cm², 1.06 W/cm² deposited at PLA/G-agarose interface. (h) Corresponding temperature profiles evaluated along z direction from the PLA/G-agarose interface.

To further validate the photothermal response, *ex vivo* chicken muscle tissues (average thickness: 3 mm) were employed as biological tissue phantoms. Samples were immersed in Tz solutions at concentrations of 0.3 M and 0.5 M and subsequently irradiated with the 808-nm laser. The resulting temperature profiles were monitored as a function of both dye concentration and laser power density (Fig. 5d). At a power density of 0.49 W/cm², minimal temperature changes were observed: the control and 0.3 M samples reached steady-state temperatures of 27.5 °C and 27.0 °C, respectively. In contrast, the 0.5 M sample exhibited a modest increase, reaching 28.6 °C. Upon increasing the power density to 0.62 W/cm², the control reached 28.0 °C, whereas samples treated with 0.3 M and 0.5 M of Tz approached temperatures of 29.3 °C and 33.4 °C, corresponding to relative increases of approximately 4.6% and 19.0%, respectively. Under the highest tested power density of 1.06 W/cm², the control reached 28.7 °C, whereas the 0.3 M and 0.5 M Tz-treated samples reached 32.0 °C and 42.0 °C, respectively. These values represent temperature increases of approximately 11% and 46%, respectively, relative to the baseline. Thermal distributions along the radial profile of Tz-treated and untreated chicken models are shown in Fig. S5.

Nonlinear curve fitting was performed to retrieve the parameter (λ) associated with thermal diffusion was extracted based on the applied model equation:

$$T(t) = T_{\infty} - (T_{\infty} - T_0)e^{-\lambda t} \quad (6)$$

where T_{∞} is the steady-state temperature, T_0 is the temperature at 0 s. The treatment with Tz was found to significantly influence the thermal response. Specifically, the λ value increased as the power density increased, proportionally to the concentration of Tz with which the *ex vivo* model was treated (Fig. 5e).

A computational model was developed to simulate the thermal behavior of a layered system composed of a PLA/G composite disk of diameter 2 mm and thickness 0.5 mm positioned at the bottom of a cylindrical geometry of diameter 10 mm. Above the disk, a cylinder of agarose gel (4-mm thick) and a cylinder of cell culture medium (4-mm thick) were placed (Fig. 5f). The setup aimed to mimic experimental conditions for laser-induced heating. Simulations were conducted to evaluate the temperature distribution within the system under different laser power densities (0.37 W/cm², 0.49 W/cm², 0.62 W/cm², 0.75 W/cm², and 1.06 W/cm²). As shown in Fig. 5g, an increase in the laser power density leads to an increase in the steady-state temperature, with a thermal gradient ranging from 5 °C/mm to 19 °C/mm moving away from the PLA/G interface (Fig. 5h).

Efficacy of photothermal therapy on cancer cells

To study the impact of Tz in photothermal therapies, we built a tumor-tissue interface model as shown in Fig. 6a. The glioblastoma models (GBM) were 3D bioprinted on biocompatible PLA/G scaffolds and immersed in cell culture medium, whereas Tz-treated and untreated tissue-like models were placed between tumor models and laser source. We used laser power densities of 0.37 W/cm², 0.62 W/cm², and 1.06 W/cm² to explore different photothermal regimes: physiological conditions, MPTT, and PTT^{11,12}. Figure 6b shows representative fluorescence images of the glioblastoma models after different irradiation conditions, in which viable and dead cells were selectively labelled with calcein ($\lambda_{\text{exc}} = 495$ nm, $\lambda_{\text{em}} = 515$ nm) and PI ($\lambda_{\text{exc}} = 535$ nm, $\lambda_{\text{em}} = 617$ nm), respectively. Under these same irradiation conditions, temperature measurements revealed that the presence of Tz increased the temperature up to + 10 °C compared to untreated models, resulting in peak temperatures around 55 °C within the GBM constructs. At the lowest irradiation level (0.37 W/cm²), the delivered optical power is insufficient to overcome thermal diffusion within the medium, which rapidly dissipates the deposited heat. As a consequence, no appreciable temperature rise occurs in either the untreated or the Tz-treated samples, leading to identical temperatures under these conditions.

Two hours after irradiation, we observed a negligible variation of cell viability moving from 0.37 W/cm² to 0.62 W/cm² in Tz-untreated samples, whereas only a 15.4% reduction in cell viability under 1.06 W/cm² laser stimulus (Fig. 6c). In contrast, Tz-treated samples exhibit more robust reductions of cell viability even at a more modest laser power of 0.62 W/cm² (13.3% reduction) with a 42.4% reduction at 1.06 W/cm² as a consequence of the higher temperature approached (Fig. 6c). Quantitative analysis of cell death revealed a progressive increase in the fraction of apoptotic cells with increasing laser power, which was markedly higher in Tz-treated than in untreated samples up to 4.4-fold (Fig. 6d). Consistently, we observed a power-dependent rise in ROS levels, with a pronounced ROS overproduction up to 2.66-fold in Tz-treated constructs exposed to 1.06 W/cm² (Fig. 6e). These findings are consistent with previous reports on conventional PTT, which suggest that effective therapeutic effects generally require temperatures above 45 °C³⁵.

Conclusions

In this study, we demonstrated that a strongly absorbing molecule such as Tz can counterintuitively reduce biological tissue scattering through RI modulation, thereby potentially enhancing the effectiveness of PTTs. Through *in silico* wavefront propagation and thermal diffusion analysis, as well as *in vitro* and *ex vivo* experimental validations, we showed that Tz significantly reduces optical scattering, leading to increased light penetration and improved energy delivery to deep tissue layers.

This reduced scattering translates into two critical clinical benefits: (i) for the same dose, deeper penetration can be achieved, and (ii) for the same depth, a lower energy dose is required, therefore reducing collateral damage to surrounding healthy tissue. Furthermore, the reduction in tissue scattering allows for a decrease in the required concentration of photo-absorbers, which may mitigate potential cytotoxicity concerns while preserving therapeutic efficacy.

Additionally, the enhanced beam homogeneity ($\sim 98.9\%$ from *in silico* models) minimizes the formation of hot and cold spots, ensuring a more uniform thermal dose per unit area. This aspect is particularly advantageous in treatments involving large and highly heterogeneous tissue volumes, where conventional approaches often suffer from uneven energy distribution due to scattering. Indeed, Tz reduces dose variability across the target,

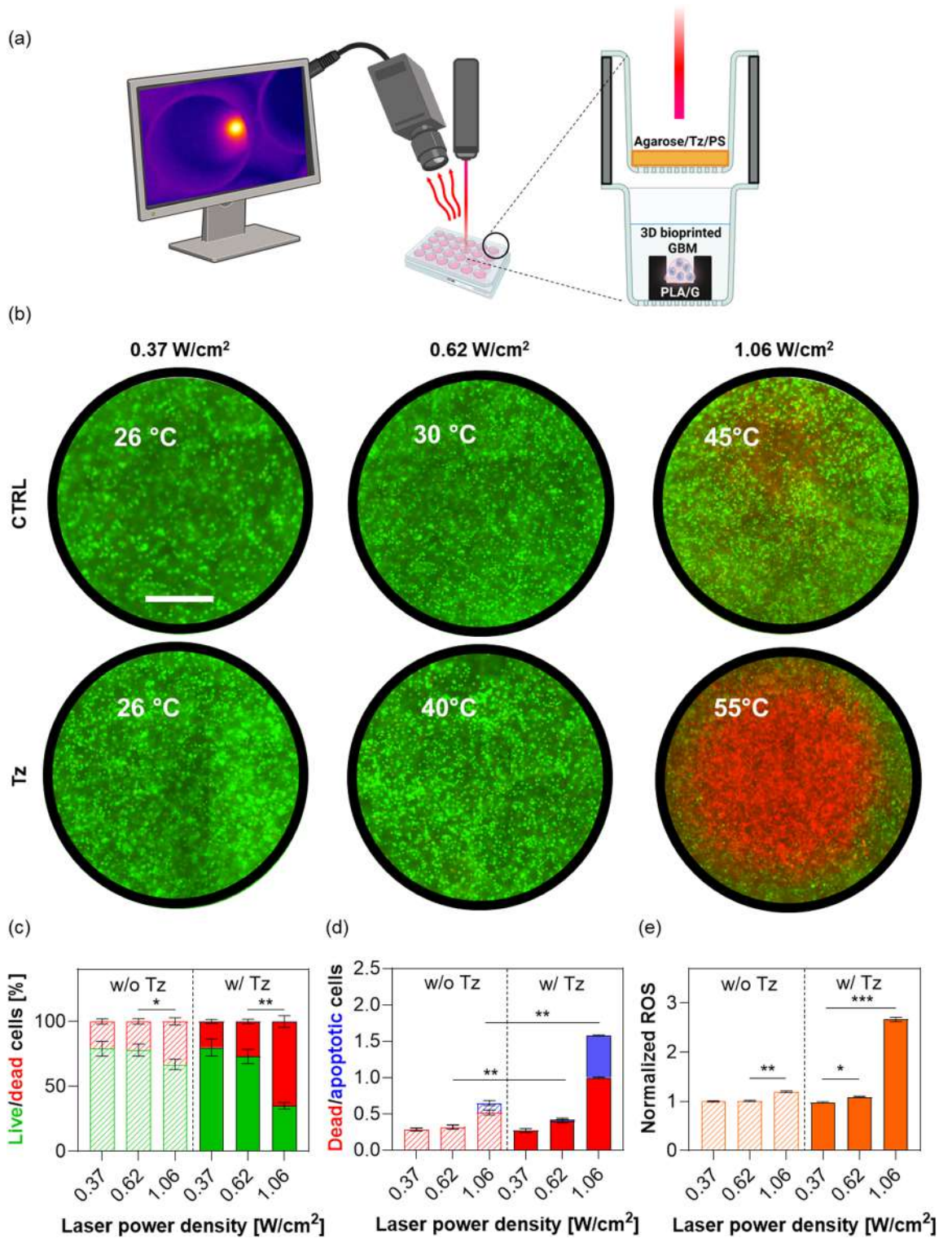


Fig. 6. (a) Experimental setup consisting of 808-nm laser and thermal camera that point at the tumor-tissue interface model. The inset shows a scheme of the tumor-tissue model made of a Tz-treated (or untreated) scattering agarose phantom positioned over the GBM tumor model (not in contact), which was 3D bioprinted onto a PLA/G scaffold and immersed in cell culture medium. (b) Calcein/PI stained GBM models after 2 h post NIR irradiation at different laser power densities. Scale bar: 10 mm. Corresponding histograms of (c) calcein/PI integrated fluorescence intensities, (d) dead/apoptotic cells, and (e) production of reactive oxygen species (ROS) after NIR irradiation. Data are reported as mean value on three independent measurements. Statistical significance was evaluated using two-way ANOVA test (* $p < 0.05$; ** $p < 0.01$; *** $p < 0.001$).

lowering the risk of over- or under-treatment in specific regions, while offering the added benefit of being a reversible and non-permanent intervention that does not induce long-term structural changes in the tissue.

Despite these promising findings, some limitations should be acknowledged. First, our characterizations were performed under controlled in vitro and ex vivo conditions, which may not fully replicate the complexity of the in vivo tumor microenvironment. This choice, however, was deliberate and consistent with the proof-of-concept nature of the study. By using 3D-bioprinted GBM models and tissue-mimicking phantoms, we aimed to reproduce key optical and structural features of in-vivo tissues while adhering to the 3R principles (Replacement, Reduction, Refinement). Second, although we used Tz at concentrations and exposure times consistent with those reported in recent in vivo optical-clearing literature^{21,23,36,37}, where minimal systemic toxicity was observed in long-term studies²³, our approach is conceived to be topical and transient, with Tz present ideally only during the 3-minute irradiation window. As such, our method is not intended for systemic uptake or cellular internalization, and toxicity concerns at the cell-intrinsic level are less relevant; however, comprehensive toxicological studies will still be required before translation^{38,39}. Finally, the precise molecular interactions of Tz with ECM components and their possible influence on tumor physiology are not yet fully understood.

Future work should therefore focus on in vivo investigations to validate whether the optical clearing effects of Tz translate into measurable therapeutic gains in animal models of deep-seated tumors. Such studies will be essential to assess not only therapeutic efficacy, but also pharmacokinetics, biodistribution, and systemic tolerability. Moreover, integrating Tz-mediated clearing with advanced light-delivery strategies (e.g., interstitial fiber optics or multiphoton excitation) could expand its utility beyond superficial lesions. Exploring synergistic combinations with immunotherapies or drug delivery platforms may also help maximize the translational impact of this approach.

Definitively, modulating tissue optical properties via RI matching may potentially unlock new pathways for safer, deeper, and more uniform energy delivery in PTTs. Although additional validation is required, this approach holds strong translational potential and could be considered a valid strategy in future developments of clinically optimized photothermal platforms.

Data availability

The datasets analyzed during the current study available from the corresponding author on reasonable request.

Received: 15 October 2025; Accepted: 30 January 2026

Published online: 06 February 2026

References

- Diederich, C. J. Thermal ablation and high-temperature thermal therapy: overview of technology and clinical implementation. *Int. J. Hyperth.* **21**, 745–753 (2005).
- Ding, Q. et al. Rabies virus targeting NIR-II phototheranostics. *J. Am. Chem. Soc.* **147**, 16661–16673 (2025).
- Huang, X., Jain, P. K. & El-Sayed, I. H. El-Sayed, M. A. Plasmonic photothermal therapy (PPTT) using gold nanoparticles. *Lasers Med. Sci.* **23**, 217–228 (2008).
- Han, H. S. & Choi, K. Y. Advances in Nanomaterial-Mediated photothermal cancer therapies: toward clinical applications. *Biomedicines* **9**, 305 (2021).
- Perini, G. et al. Impact of different 2D materials on the efficacy of photothermal and photodynamic therapy in 3D-bioprinted breast cancer. *Nanoscale* **17**, 3221–3235 (2025).
- Ding, Q. et al. Precision phototherapy enabled by decoding complex microenvironments. *Acc. Chem. Res.* **58**, 3167–3183 (2025).
- Jaque, D. et al. Nanoparticles for photothermal therapies. *Nanoscale* **6**, 9494–9530 (2014).
- Chen, Q. et al. Photothermal therapy with immune-adjuvant nanoparticles together with checkpoint Blockade for effective cancer immunotherapy. *Nat. Commun.* **7**, 13193 (2016).
- Perini, G. et al. Slow and steady wins the race: fractionated near-infrared treatment empowered by graphene-enhanced 3D scaffolds for precision oncology. *Mater. Today Bio.* **25**, 100986 (2024).
- Ding, Q. et al. Dual-laser 808 and 1,064 nm strategy that circumvents the Achilles' heel of photothermal therapy. *Proceedings of the National Academy of Sciences* **122**, e2503574122 (2025).
- Cai, Y., Lv, Z., Chen, X., Jin, K. & Mou, X. Recent advances in biomaterials based near-infrared mild photothermal therapy for biomedical application: A review. *Int. J. Biol. Macromol.* **278**, 134746 (2024).
- Xu, N. et al. Biomedical applications and prospects of temperature-orchestrated photothermal therapy. *MedComm – Biomaterials Appl.* **1**, e25 (2022).
- Liu, Y., Bhattarai, P., Dai, Z. & Chen, X. Photothermal therapy and photoacoustic imaging via nanotheranostics in fighting cancer. *Chem. Soc. Rev.* **48**, 2053–2108 (2019).
- Cheng, L., Wang, C., Feng, L., Yang, K. & Liu, Z. Functional nanomaterials for phototherapies of cancer. *Chem. Rev.* **114**, 10869–10939 (2014).
- Mei, L. et al. Nanozymes for Non-Neoplastic diseases: catalytic therapy redefined. *Aggregate* **6**, e70150 (2025).
- Costantini, I., Cicchi, R., Silvestri, L., Vanzi, F. & Pavone, F. S. In-vivo and ex-vivo optical clearing methods for biological tissues: review. *Biomed. Opt. Express.* **10**, 5251 (2019).
- Amchova, P., Siska, F. & Ruda-Kucerova, J. Safety of tartrazine in the food industry and potential protective factors. *Heliyon* **10**, e38111 (2024).
- Miller, D. A. et al. Enhanced penetration depth in optical coherence tomography and photoacoustic microscopy in vivo enabled by absorbing dye molecules. *Optica* **12**, 24 (2025).
- Shabbir, M. W., Phillips, M., Asante-Asare, D. & Ou, Z. Transient optical clearing using absorbing molecules for ex-vivo and in-vivo imaging. *BioRxiv Preprint at* <https://doi.org/10.1101/2025.04.02.646849> (2025).
- Garbelli, M. & Chen, Z. Food dye for optical clearing and in vivo imaging. *Kidney Int.* **107**, 776–778 (2025).
- Keck, C. H. C. et al. Achieving transient and reversible optical transparency in live mice with tartrazine. *Nat. Protoc.* <https://doi.org/10.1038/s41596-025-01187-z> (2025).
- De Maio, F. et al. 3D-printed graphene polylactic acid devices resistant to SARS-CoV-2: Sunlight-mediated sterilization of additive manufactured objects. *Carbon N Y.* **194**, 34–41 (2022).
- Ou, Z. et al. Achieving optical transparency in live animals with absorbing molecules. *Sci. (1979)*. **385**, eadm6869 (2024).

24. Welvaert, M. & Rosseel, Y. On the definition of Signal-To-Noise ratio and Contrast-To-Noise ratio for fMRI data. *PLoS One*. **8**, e77089 (2013).
25. Gu, W. Y., Yao, H., Vega, A. L. & Flagler, D. Diffusivity of ions in agarose gels and intervertebral disc: effect of porosity. *Ann. Biomed. Eng.* **32**, 1710–1717 (2004).
26. Shaw, C., Hossain, K., Riviere-Cazaux, C., Burns, T. & Khan, M. R. Convection-enhanced diffusion and directed withdrawal of methylene blue in agarose hydrogel using finite element analyses. *bioRxiv* 10.27.514109 Preprint at (2022). <https://doi.org/10.1101/2022.10.27.514109> (2022).
27. Menikou, G. & Damianou, C. Acoustic and thermal characterization of agar based phantoms used for evaluating focused ultrasound exposures. *J. Ther. Ultrasound*. **5**, 14 (2017).
28. Ed-Daoui, A., Benelmostafa, M. & Dahmani, M. Study of the viscoelastic properties of the agarose gel. *Mater. Today Proc.* **13**, 746–751 (2019).
29. Minopoli, A. et al. Viscoelastic interpretation of AFM nanoindentation for predicting nanoscale stiffness in soft biomaterials. *Polym. Test.* **153**, 109026 (2025).
30. Distler, T., Schaller, E., Steinmann, P., Boccaccini, A. R. & Budday, S. Alginate-based hydrogels show the same complex mechanical behavior as brain tissue. *J. Mech. Behav. Biomed. Mater.* **111**, 103979 (2020).
31. Fannon, O. M., Bithell, A., Whalley, B. J. & Delivopoulos, E. A fiber alginate Co-culture platform for the differentiation of mESC and modeling of the neural tube. *Front Neurosci* **14**, 524346 (2021).
32. Naglič, P., Zelinsky, Y., Likar, B. & Bürmen, M. Determination of refractive index, size, and solid content of monodisperse polystyrene microsphere suspensions for the characterization of optical phantoms. *Biomed. Opt. Express*. **11**, 1901 (2020).
33. He, G. S., Qin, H. Y. & Zheng, Q. Rayleigh, Mie, and Tyndall scatterings of polystyrene microspheres in water: Wavelength, size, and angle dependences. *J. Appl. Phys.* **105**, 023110 (2009).
34. Arslan, H. & Dolukan, Y. B. Optical penetration depths and fluence distributions in chicken breast and liver tissues. *Opt. Spectrosc.* **127**, 763–768 (2019).
35. Wang, P. et al. Enhancing the efficiency of Mild-Temperature photothermal therapy for cancer assisting with various strategies. *Pharmaceutics* **14**, 2279 (2022).
36. Jia, C. et al. Tartrazine-enabled optical clearing for in vivo optical resolution photoacoustic microscopy. *Biomed. Opt. Express*. **16**, 2504 (2025).
37. Miller, D. A. et al. Enhanced penetration depth in optical coherence tomography and photoacoustic microscopy *in vivo* enabled by absorbing dye molecules. *Optica* **12**, 24 (2025).
38. Visternicu, M. et al. Toxicological effects of tartrazine exposure: A review of in vitro and animal studies with human health implications. *Toxics* **13**, 771 (2025).
39. Zand, A. et al. The impact of tartrazine on DNA Methylation, histone Deacetylation, and genomic stability in human cell lines. *Nutrients* **17**, 913 (2025).

Acknowledgements

We acknowledge financial support under the National Recovery and Resilience Plan (NRRP), Mission 4, Component 2, Investment 1.1, Call for tender No. 1409 published on 14.9.2022 by the Italian Ministry of University and Research (MUR), funded by the European Union – NextGenerationEU– Project Title Graphene Quantum Dots-Mediated Photoimmunotherapy Against Glioblastoma in a Bioprinted Mini-Brain-on-Chip – CUP B53D23031470001. VP acknowledges financial support from Piano Nazionale per gli Investimenti Complementari al PNRR (PNC - Avviso D.D. n. 931 del 06/06/2022), Project D3 4 HEALTH - Digital Driven Diagnostics, prognostics and therapeutics for sustainable Health care -PNC0000001, CUP B53C22006100001. MP acknowledges financial support from AIRC under IG 2024—ID. 30398 project. GP acknowledges financial support under the National Recovery and Resilience Plan (NRRP), Mission 4, Component 2, Investment 1.1, Call for tender No. 1409 published on 14.9.2022 by the Italian Ministry of University and Research (MUR), funded by the European Union – NextGenerationEU– Project Title Graphene Quantum Dots-Mediated Photoimmunotherapy Against Glioblastoma in a Bioprinted Mini-Brain-on-Chip – CUP J53D23017940001. We acknowledge the contribution of 3D Bioprinting Research Core Facility G-STeP of the Fondazione Policlinico Universitario A. Gemelli IRCCS for sample processing and the G-STeP Microscopy Facility of the Fondazione Policlinico Universitario A. Gemelli IRCCS for microscopy experiments.

Author contributions

M.P. and V.P. conceived and designed the study. A.M., A.A., D.E. and M.M. performed the experiments and collected the data. A.M. and G.P. developed the methodology and performed formal analysis. A.M. contributed software and validation. A.M., G.P. handled data curation and visualization. A.M., D.E., and M.M. interpreted the results and drafted the manuscript. V.P., M.P., and M.D.S. supervised the project and acquired funding. All authors reviewed and approved the final manuscript.

Funding

We acknowledge financial support under the National Recovery and Resilience Plan (NRRP), Mission 4, Component 2, Investment 1.1, Call for tender No. 1409 published on 14.9.2022 by the Italian Ministry of University and Research (MUR), funded by the European Union – NextGenerationEU– Project Title Graphene Quantum Dots-Mediated Photoimmunotherapy Against Glioblastoma in a Bioprinted Mini-Brain-on-Chip – CUP B53D23031470001. VP acknowledges financial support from Piano Nazionale per gli Investimenti Complementari al PNRR (PNC - Avviso D.D. n. 931 del 06/06/2022), Project D3 4 HEALTH - Digital Driven Diagnostics, prognostics and therapeutics for sustainable Health care -PNC0000001, CUP B53C22006100001. MP acknowledges financial support from AIRC under IG 2024—ID. 30398 project. GP acknowledges financial support under the National Recovery and Resilience Plan (NRRP), Mission 4, Component 2, Investment 1.1, Call for tender No. 1409 published on 14.9.2022 by the Italian Ministry of University and Research (MUR), funded by the European Union – NextGenerationEU– Project Title Graphene Quantum Dots-Mediated Photoimmunotherapy Against Glioblastoma in a Bioprinted Mini-Brain-on-Chip – CUP J53D23017940001. We acknowledge the contribution of 3D Bioprinting Research Core Facility G-STeP of the Fondazione Policlinico Universitario A. Gemelli IRCCS for sample processing and the G-STeP Microscopy Facility of the Fondazione Policlinico

Universitario A. Gemelli IRCCS for microscopy experiments.

Declarations

Competing interests

The authors declare no competing interests.

Additional information

Supplementary Information The online version contains supplementary material available at <https://doi.org/10.1038/s41598-026-38616-2>.

Correspondence and requests for materials should be addressed to V.P. or M.D.S.

Reprints and permissions information is available at www.nature.com/reprints.

Publisher's note Springer Nature remains neutral with regard to jurisdictional claims in published maps and institutional affiliations.

Open Access This article is licensed under a Creative Commons Attribution-NonCommercial-NoDerivatives 4.0 International License, which permits any non-commercial use, sharing, distribution and reproduction in any medium or format, as long as you give appropriate credit to the original author(s) and the source, provide a link to the Creative Commons licence, and indicate if you modified the licensed material. You do not have permission under this licence to share adapted material derived from this article or parts of it. The images or other third party material in this article are included in the article's Creative Commons licence, unless indicated otherwise in a credit line to the material. If material is not included in the article's Creative Commons licence and your intended use is not permitted by statutory regulation or exceeds the permitted use, you will need to obtain permission directly from the copyright holder. To view a copy of this licence, visit <http://creativecommons.org/licenses/by-nc-nd/4.0/>.

© The Author(s) 2026